13th ewtec 2019 Proceedings of the 13th European Wave and Tidal Energy Conference 1-6 Sept 2019, Naples, Italy

Contribution to the CCP-WSI Blind Test Series 2: CFD-based numerical wave tank experiments employing an impulse source wave maker

Christian Windt, Josh Davidson, Pál Schmitt and John V. Ringwood

***Abstract*—During the development and optimisation of wave energy converters, numerical wave tanks are useful tools, providing detailed insight into the hydrodynamic performance of devices. Specifically, computational fluid dynamics based numerical wave tanks can deliver high-fidelity, high resolution, results for a wide range of test conditions. However, CFD-based numerical wave tanks come at significant computational cost and require more man-hours during model setup, compared to lower-fidelity, frequency domain based models. The computational costs can only be significantly decreased by improving the numerical solvers, or increased expenditure on computational power. The required man-hours for the model setup, however, can be reduced by streamlining the setup of CFD-based numerical wave tanks. To this end, the formulation of best-practice guidelines and benchmark test cases can expedite this streamlining. A step towards such best-practice guidelines, and, furthermore, towards an increased confidence in CFD-based numerical wave tanks, are blind tests. This paper presents the CFD-based numerical wave tank used for the authors' contribution to the *Collaborative Computational Project in Wave Structure Interaction* Blind Test Series 2. In the employed numerical wave tanks, a recently developed, self-calibrating, impulse source wave maker is implemented for the wave generation [1]. In addition to the required data for the submission to the blind test, the paper contains preliminary studies on the necessity of turbulence modelling, spatial and temporal convergence studies, as well as results for the numerical wave maker calibration.**

***Index Terms*—Collaborative Computational Project in Wave Structure Interaction (CCP-WSI), Blind Test, Impulse wave maker, CFD-based numerical wave tank, OpenFOAM**

I. Introduction

In the field of marine renewable energy, and specifically wave energy, numerical wave tanks (NWTs) are commonly used tools for device design and optimisation. Depending on the implemented equations for the solution of the wave-structure interaction (WSI) problem, different levels of fidelity, at different levels of computational cost, can be achieved [2]. Lower-fidelity models, implementing methods based on the Laplace equation and, thus, neglecting non-linear effects, such as viscosity, are associated with minimal computational cost and are valuable tools for parametric studies or extensive-search optimisation algorithms. However, due to the required linearisation of the hydrodynamic equations, lower-fidelity models are only valid when considering linear conditions, i.e. small amplitude waves and device motions.

Contrary, higher-fidelity NWTs, such as CFD-based numerical wave tanks (CNWTs), are able to capture all relevant hydrodynamic non-linearities, by numerically solving the Reynolds Averaged Navier-Stokes equations (RANSE). Thus, CNWTs are valid over a wide range of test conditions, and are particularly valuable when modelling wave energy converters (WECs) under controlled conditions [3], [4]. Under controlled conditions, an energy maximising controller drives the WEC into resonance with the incident wave, resulting in enhanced device motion, pushing linear hydrodynamic models beyond their validity limits.

Although high-fidelity non-linear hydrodynamic models, such as CNWTs, are essential when modelling non-linear WSI or controlled WECs, these models are not yet widely used, and are only recently gaining application in the marine renewable energy field, due to:

(1) Relatively long run times
(2) Long setup time for CNWT models
(3) Requirement of specialised engineers for the model setup
(4) Lack of confidence in CNWT models

While the run times will always be significantly longer than for lower-fidelity models, points (2)–(4) can be improved by defining guidelines and standards for CNWTs in marine renewable energy applications.

One step towards such guidelines and standards are blind tests for model validation. High quality experiments in physical wave tanks (PWTs) are performed, and relevant measurements (e.g. free surface elevation (FSE) and device motion) are recorded. Participants of the blind tests are given information on the physical set-up (tank dimensions, measurement location, body mass, etc.), in order to replicate the experiment with their CNWT. The results of the CNWT simulation (e.g. FSE and device motion) are then submitted for a blind comparison to the reference results from the physical experiments. This procedure prevents *tuning* of numerical models to fit known experimental tank

Paper ID: 1265 Conference track: WHM

C. Windt and J. V. Ringwood are with the Department of Electronic Engineering, Centre for Ocean Energy Research, Maynooth University, Maynooth, Co. Kildare, Ireland (christian.windt.2017@mumail.ie; john.ringwood@mu.ie)

J. Davidson is with the Department of Fluid Mechanics, Faculty of Mechanical Engineering, Budapest University of Technology and Economics, Hungary (e-mail: davidson@ara.bme.hu)

P. Schmitt is with the Marine Research Group, Queen's University Belfast (e-mail: p.schmitt@qub.ac.uk)

 Copyright © European Tidal and Wave Energy Conference 2019

test results, thereby undermining the confidence and generalisation ability of the numerical models.

Recently, a series of blind tests have been conducted as part of the *Collaborative Computational Project in Wave Structure Interaction* (CCP-WSI). A first test series, Blind Test Series 1, considered a fixed floating production storage and offloading unit exposed to focused waves [5]. Results were presented in conjunction with the *International Society of Offshore and Polar Engineers* (ISOPE) conference, 2018. In a second [6] and third [7] series of the CCP-WSI Blind Tests, moving, WEC-like, structures (see Figs. 1 and 3), exposed to focused waves, are considered. The FSE of the considered focused waves at the focal point are shown in Fig. 4. For Blind Test Series 2 and 3, the same WEC structures are used, but are exposed to different waves.

(a) Geometry 1 (G1) (b) Geometry 2 (G2)

Fig. 1. Geometries considered for Blind Test Series 2 and 3: G1 is a cylindrical bouy with a hemispherical bottom; G2 is a cylindrical buoy with a moon-pool. Figure adapted from [6]

In this paper, the numerical model and the results for the contribution to the CCP-WSI Blind Tests Series 2 are presented[1]. The CNWT is implemented in the open-source CFD software OpenFOAM [9]. Waves are generated using a recently developed, self-calibrating, impulse source wave maker [1]. It should be noted that this paper presents the first application of the proposed wave maker and calibration algorithm to physically measured FSE data of focused waves.

The remainder of this paper is organised as follows: The setup of the experimental tank tests will be described briefly in Section II. Next, in Section III, the setup of the CNWT is presented. The governing equations, as well as details on the implemented wave generation and absorption method, are given. Furthermore, convergence studies of the problem discretisation (spatially and temporally) are presented, and the specific solver settings and solution schemes are given. Results of the CNWT simulations are presented and discussed in Section IV. Finally, conclusions are drawn in Section V.

II. Experimental Tank Test Setup

To gain meaningful results from blind tests, high quality experimental data are a prerequisite. To this end, the organisers of the CCP-WSI Blind Test Series 2 performed experiments in the ocean basin of the COAST laboratory at Plymouth University, specifically for the purpose of CNWT validation.

[1]The contribution to the CCP-WSI Blind Test Series 3 are presented in [8]

The test campaign includes WSI, as well as wave only experiments. While the results of the wave only experiments are provided to the blind test participants, results of the WSI experiments are, at the time of writing, undisclosed.

A. Physical Wave Tank

A schematic of the PWT, with all relevant dimensions and the wave probe (WP) locations marked in red, is depicted in Fig. 2. The coordinate system in Fig. 2 coincides with the coordinate system of the CNWT. Flap type waver makers are located at the left hand side of the PWT and an absorbing, sloped, beach is located on the right hand side, 21.9m from the wave makers. The water depth is 3m in the test section.

The WEC structure is located at a distance of 14.8m to the wave paddle, and 0.278m off the centre line in the -y direction. This location coincides with the position of WP 5 in Fig. 2. In total, 13 WPs are distributed in the PWT for the wave only experiments. For the WSI experiments, WP 5 is removed.

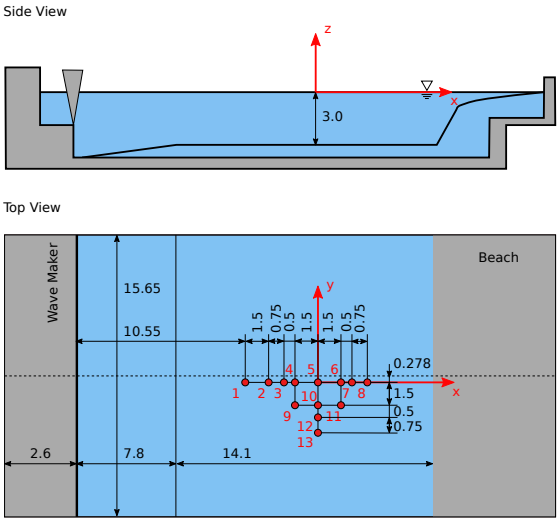

Fig. 2. Schematic (not to scale) of the PWT including the main dimensions (in meters). The red circles indicated the WP locations. The WEC structure is located at WP 5.

B. WEC Structures

For Blind Test Series 2, two different axisymmetric, cylindrical structures are considered, G1 and G2, representing point absorber type WECs. While G1 features a hemispherical bottom (see Fig. 3a), G2 features a sharp-cornered bottom and a moon-pool (see Fig. 3b). All relevant structural dimensions, as well as the mass and inertial properties of the two geometries, are shown in Fig. 3 and listed in Table I.

The mooring of the WEC structure is realised with a linear spring, connecting the device with the tank floor. The stiffness of the spring is $67\,\mathrm{N\,m^{-1}}$. The mooring pretension was measured in the PWT, with the body floating in its equilibrium position, and is listed in Table I.

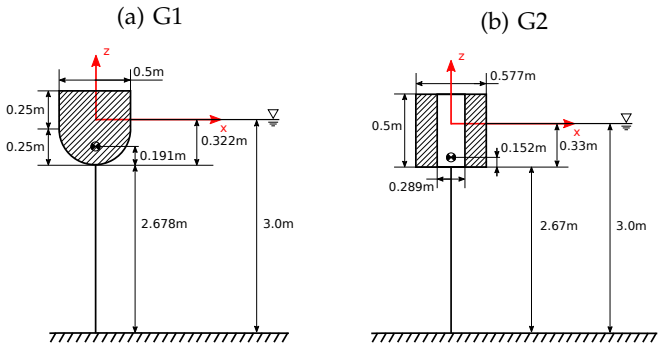

Fig. 3. Schematic (not to scale) of the two considered WEC structures including the main dimensions.

TABLE I
PROPERTIES OF THE CONSIDERED WEC GEOMETRIES

	Mass [kg]	Ixx [kg m^2]	Iyy [kg m^2]	Izz [kg m^2]	Mooring Pretension [N]
G1	43.674	1.620	1.620	1.143	32.07
G2	61.459	3.560	3.560	3.298	31.55

C. Input Waves

Three different focused waves of varying steepness are considered, 1BT2 – 3BT3[2], as listed in Table II. While the peak wave amplitude, An, and the water depth, d, are kept constant, the peak frequency, fp, varies between 0.3578Hz (1BT2), 0.4Hz (2BT2) and 0.4382Hz (3BT2), resulting in wave steepnesses of 0.129, 0.161 and 0.193, respectively.

The experimentally measured FSE for each wave, at WP 5, is plotted in Fig. 4. Note that the FSE is plotted against relative time, t_r, so that all peaks are artificially aligned at $t_r = 1$.

TABLE II
WAVE CHARACTERISTICS OF THE THREE CONSIDERED FOCUSED WAVES (FOCUSED LOCATION AT LOCATION OF WAVE PROBE 5)

	An [m]	fp [Hz]	d [m]	Hs [m]	λ [m]	kA [-]
Wave 1BT2	0.25	0.3578	3.0	0.274	11.35	0.129
Wave 2BT2	0.25	0.4	3.0	0.274	9.41	0.161
Wave 3BT2	0.25	0.4382	3.0	0.274	7.99	0.193

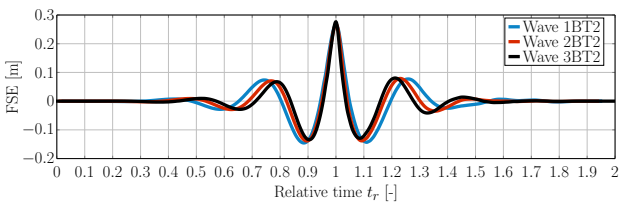

Fig. 4. FSE of the considered focused waves (1BT2–3BT2) at the focal location. The time traces are artificially aligned to match the peaks at $t_r = 1$.

[2]The labelling of the waves is based on the nomenclature in [6].

III. Numerical Wave Tank Setup

The CNWT model in this study is based on the open-source CFD software OpenFOAM [9], specifically version 4.1 of the OpenFOAM Foundation fork [10]. The hydrodynamics in the CNWT are captured by solving the incompressible RANSE, describing the conservation of mass

$$\nabla \cdot \mathbf{U} = 0 \tag{1}$$

and momentum

$$\frac{\partial \rho \mathbf{U}}{\partial t} + \nabla \cdot \rho \mathbf{U}\mathbf{U} = -\nabla p + \nabla \cdot \mathbf{T} + \rho \mathbf{f}_b \,. \tag{2}$$

In (1) and (2), t denotes time, $\mathbf{U}$ is the fluid velocity, p the fluid pressure, ρ the fluid density, $\mathbf{T}$ the stress tensor, and $\mathbf{f}_b$, the external forces, such as gravity.

The water wave advection is captured via the volume of fluid (VOF) method, proposed in [11], following

$$\frac{\partial \alpha}{\partial t} + \nabla \cdot (\mathbf{U}\alpha) + \nabla \cdot [\mathbf{U_r}\alpha(1-\alpha)] = 0 \tag{3}$$

$$\Phi = \alpha \Phi_{\text{water}} + (1-\alpha)\Phi_{\text{air}} \,, \tag{4}$$

where α denotes the volume fraction of water, U_r is the relative velocity between liquid and gaseous phase [12], and Φ is a specific fluid quantity, such as density.

To measure the FSE, the iso-surface of the volume fraction $\alpha = 0.5$ is recorded throughout the course of the simulation. The FSE at specific locations, which follow the layout of the PWT (see Fig. 2), are then extracted from the iso-surface data in a post-processing step.

D. Spatial and Temporal Discretisation

To determine the spatial and temporal problem discretisation sizes, convergence studies have been performed, preliminary to the final simulations for the blind test. As a test case, geometry G1, exposed to the focused wave 1BT2, has been chosen. Simulations are run for three different discretisation sizes, i.e. three different grid sizes in the free surface interface zone and around the body, for the spatial convergence study, and three different time steps sizes for the temporal convergence study[3]. The results for the translational (heave and surge) and rotational (pitch) motion are depicted in Figs. 5 and 6, for the spatial and temporal convergence study, respectively.

Visual inspection of the time traces in Figs. 5 and 6 shows that converged results are achieved for the motion of the geometry. For the spatial convergence study, all the plotted results show converged results with a grid size of 10 cells per wave height of wave 1BT2 (see the grid layout in Fig. 7). Similarly, for the temporal problem discretisation, converged results are achieved with a time step size of $\Delta t = 0.002\,\text{s}$.

[3]Note that fixed time step sizes, rather than variable time step sizes with a Courant number criterion, have been used for the subsequent simulations. The fixed time steps result in a consistently stable performance of the motion solver, while any potential Courant numbers > 1 are accounted for by the PIMPLE algorithm (see Section III-E).

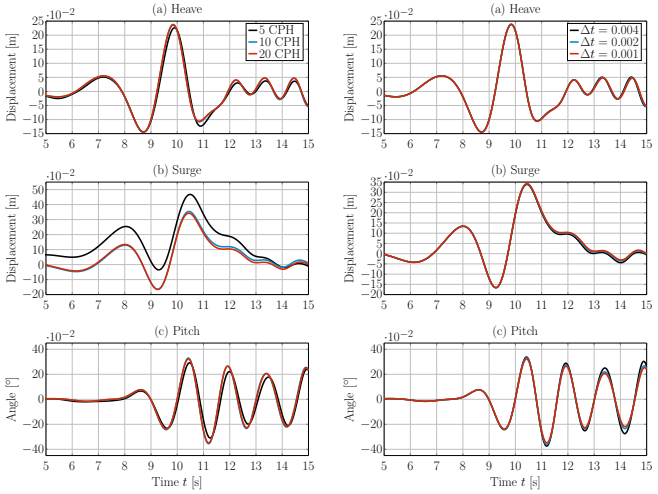

Fig. 5. Motion time traces of G1, exposed to wave 1BT2, for three different cell sizes, i.e. 5, 10 and 20 cells per wave height of wave 1BT2.

Fig. 6. Motion time traces of G1, exposed to wave 1BT2, for three different time steps, i.e. $\Delta t = 0.001, 0.002, 0.004$.

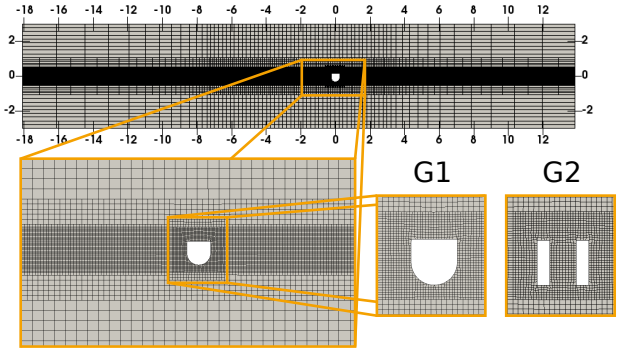

Fig. 7. Spatial discretisation of the CNWT with 10 cells per wave height for 1BT2, in the vicinity of the WEC geometry. Mesh grading is employed towards the left and right hand side domain boundary to increase the absorption efficiency of the numerical beach.

E. Solution Schemes and Solver Settings

In OpenFOAM, users can select solution schemes and tune solver settings specifically to the simulation at hand. For the cases herein, the solution schemes and solver settings are chosen based on user experience and appropriate related tutorial cases. Table III lists the solution schemes for the time differentiation, the gradient, and the divergence for selected quantities. For more information, see [13]–[15].

To determine the required minimum number of iterations in the PIMPLE algorithm, for the pressure-velocity coupling [16], preliminary simulations with varying numbers of iterations have been performed. The results for the heave displacement of geometry G1, exposed to wave 1BT2, is plotted in Fig. 8. Converged results are found with 2 iterations in the PIMPLE algorithm.

TABLE III
SOLUTION SCHEMES

	Scheme
$\partial/\partial t$	Euler
$\nabla\Phi$	Gauss linear
$\nabla \cdot \rho\mathbf{U}\mathbf{U}$	Gauss vanLeerV
$\nabla \cdot \mathbf{U}\alpha$	Gauss vanLeer
$\nabla \cdot [\mathbf{U_r}\alpha(1-\alpha)]$	Gauss interfaceCompression
$\nabla \cdot \mathbf{U}k$	Gauss upwind
$\nabla \cdot \mathbf{U}\omega$	Gauss upwind

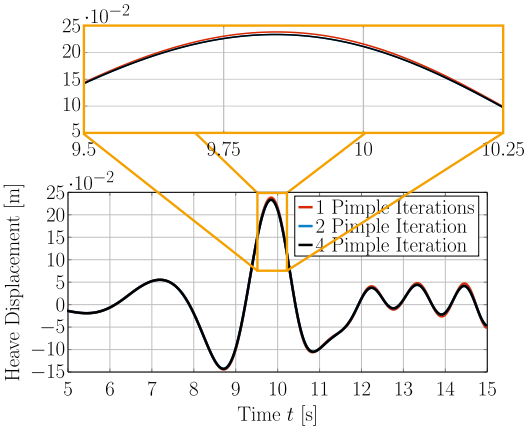

Fig. 8. Heave motion time trace of geometry G1 exposed to wave 1BT2 with three different numbers of PIMPLE iterations

F. Numerical Wave Generation and Absorption

Various numerical wave makers are available to generate and absorb waves in a CNWT [17]. For the present study, the impulse source method, presented in [1], is employed. For the impulse source wave maker, a source term, $\mathbf{r}\rho\mathbf{a_{wm}}$, is added to the RANS momentum equation (2), yielding:

$$\frac{\partial \rho \mathbf{U}}{\partial t} + \nabla \cdot \rho \mathbf{U}\mathbf{U} = -\nabla p + \nabla \cdot \mathbf{T} + \rho \mathbf{f}_b + \mathbf{r}\rho\mathbf{a_{wm}} \quad (5)$$

The location of the wave maker zone is defined by $\mathbf{r} = 1$, with $\mathbf{r} = 0$ everywhere else in the domain. $\mathbf{a}_{wm}$ is the acceleration input to the wave maker, which can be determined analytically, for shallow water waves [18] or, as applied here, via an iterative calibration, as implemented in [1].

To calibrate, $\mathbf{a}_{wm}$, a standard spectral analysis method, based on [19], is adapted to produce a target wave at a specific position within the CNWT, comprising the following steps:

1) Definition of a target wave, η_T
2) Perform a Fast Fourier Transform (FFT) on η_T, to obtain the amplitudes and phases, for each frequency component
3) Definition of an initial time series for $\mathbf{a}_{wm,1}$
4) Perform a FFT on $\mathbf{a}_{wm,1}$, to obtain the amplitudes and phases for each frequency component of $\mathbf{a}_{wm,1}$
5) Run the OpenFOAM simulation for calibration iteration i, using $\mathbf{a}_{wm,i}$, and monitor the resulting FSE, $\eta_{R,i}$, at the specific CNWT location. Note

that, for long crested waves, simulations can be performed in two-dimensional domains, in order to reduce the computational burden.

6) Perform a FFT on $\eta_{R,i}$, to obtain the amplitudes and phases for each frequency component of $\eta_{R,i}$
7) Correction of the amplitude components of $\mathbf{a}_{wm,i}$, by scaling with the ratio of the η_T and $\eta_{R,i}$ amplitudes
8) Correction of the phase components of $\mathbf{a}_{wm,i}$, by summing the phase with the difference between the phase components of η_T and $\eta_{R,i}$
9) Construction of $\mathbf{a}_{wm,i+1}$, using the Inverse Fourier Transform on the corrected amplitude and phase components
10) Steps 5 - 9 are repeated either for a maximum number of iterations, or until a threshold for the root mean-squared error (RMSE) between the η_T and $\eta_{R,i}$ is reached.

A schematic of the calibration procedure is depicted in Fig. 9. For further details, the interested reader is referred to [1].

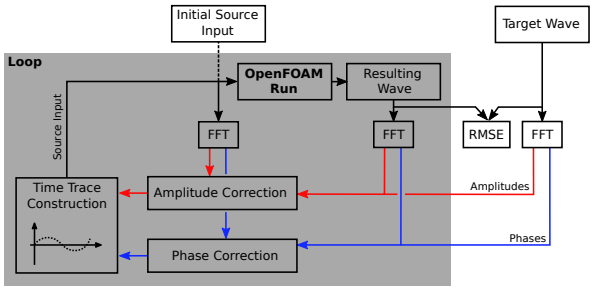

Fig. 9. Calibration scheme for the impulse source input (Figure adapted from [1])

For wave absorption, a numerical beach, proposed in [20], is implemented. Introducing the additional term, $\mathbf{S}\rho\mathbf{U}$, to the RANS momentum equation (2), yields:

$$\frac{\partial \rho \mathbf{U}}{\partial t} + \nabla \cdot \rho \mathbf{U}\mathbf{U} = -\nabla p + \nabla \cdot \mathbf{T} + \rho \mathbf{f}_b + \mathbf{S}\rho\mathbf{U} \qquad (6)$$

Here, $\mathbf{S}\rho\mathbf{U}$ describes a dissipation term, used to implement an efficient numerical beach, where the variable field $\mathbf{S}$ controls the strength of the dissipation, with a value of zero in the simulation zone, and then gradually increasing towards the boundary, over the length of the numerical beach.

To control the absorption quality of the numerical beach, the length and the maximum damping factor, $S_{\max}$, can be adjusted. For the present case, preliminary studies were performed to identify efficient beach settings for the focused waves. Based on the findings in [17], the beach length was set to $\lambda_{1\mathrm{BT2}}$, i.e. the longest wave length, and different $S_{\max}$ values were tested. The reflection coefficient, being the ratio between the incident and reflected wave field, is determined using the three point method, proposed in [21]. The results, for varying $S_{\max}$, are listed in Table IV, from which $S_{\max} = 3\mathrm{s}^{-1}$ is chosen for all subsequent simulations. Screen–shots of the side and top view of the CNWT, showing the field variable α and $\mathbf{r}$, are depicted in Fig. 10, and the field variable $\mathbf{S}$, in Fig. 11.

TABLE IV
REFLECTION COEFFICIENTS FOR DIFFERENT VALUES OF S_{MAX}

$S_{\max}$	$[\mathrm{s}^{-1}]$	3	4	5	6
1BT2	[%]	1.9	2.7	3.3	7.0
2BT2	[%]	0.5	0.6	0.9	1.0
3BT2	[%]	3.4	3.6	3.8	4.3

Note that symmetry is exploited, so only half of the PWT is modelled in the CNWT. A symmetry boundary condition is employed in the x,z-plane, where x points in the wave propagation direction, and -z towards the tank floor. Symmetry furthermore implies constraints on the allowed body motion. Here, only three degrees of freedom are allowed, i.e. heave, surge and pitch. In the PWT, no motion constraints are applied. Thus, any asymmetric effects which may occur in the PWT can not be captured in the CNWT. However, since only long crested focused waves are considered, minimising asymmetric effects, the reduced computational burden justifies the use of the symmetry boundary condition.

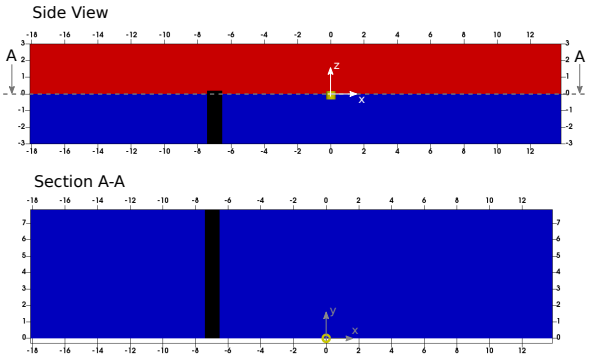

Fig. 10. Screen–shot of the CNWT including colour coding for the α field variable (blue and red), and the impulse source (black). The centre of impulse source is located at $x = -7\mathrm{m}$ with a length of $\lambda_{2\mathrm{BT2}}/10$. The geometry is located at $(0, 0, 0)$.

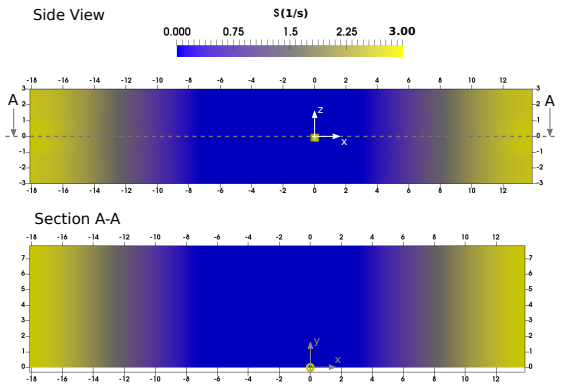

Fig. 11. Screen–shot of the CNWT including colour coding for the $\mathbf{S}$ field variable. The beach length is set to $1\lambda_{1\mathrm{BT2}}$, with a $S_{\max} = 3\mathrm{s}^{-1}$. The WEC geometry is located at $(0, 0, 0)$.

G. Turbulence Modelling

To evaluate if turbulence modelling is required, preliminary simulations are performed. For the three different input waves and the two WEC structures, simulations with and without turbulence modelling were run, and results were compared. For the turbulence modelling, a standard k-ω SST turbulence model [22] was chosen, based on the review in [23].

To allow the use of wall functions, the grid layout in the vicinity of the geometries is adjusted, compared to Fig. 7 [24]. Standard wall functions for the turbulent kinetic energy k, the turbulence frequency ω and the eddy viscosity ν are used.

To ensure the wall function validity, y^+ values should be inspected. y^+ is defined as $u_* \cdot y/\nu$, where u_* describes the friction velocity, y is the distance to the nearest wall, and ν denotes the kinematic viscosity. According to [15], the applicability of wall functions is valid for $20 \leq y^+ \leq 350$. However, as pointed out in [24], in oscillating flows, the value of y^+ changes through a wave cycle and, thus, no single grid size can be found to comply with the requirements posed on y^+. For illustrative purposes, Fig. 12 shows y^+ on the wall of G2, for wave 3BT2, at three different time instances: immediately before the focused wave crest (9s), at the focused wave crest (10s) and immediately after the focused wave crest (11s). It can be seen that, dependent on the instantaneous velocities at the wall, y^+ changes. The time-variance of y^+ and, thus, the time-varying validity of wall functions, must be considered when analysing simulations of oscillating flows which include turbulence modelling.

By way of example, Fig. 13 shows the translational and rotational motion, as well as the mooring force time traces of G2, for waves 3BT2, plotting results, with (dashed red) and with-out (solid black) turbulence modelling. Table V lists the relative deviation[4] of the peak value (as defined for the blind test submission [6]) between the simulation results with and without turbulence modelling, for G2 in all three waves.

The results indicate that including turbulence modelling mainly affects the surge and pitch motion, with maximum differences of -2.7% and 3.9%, respectively. Although the inclusion of turbulence modelling is observed to produce some differences in the results, laminar conditions are assumed for the final simulations of the blind test. This is justified by the uncertain validity of the applied wall functions, together with the increased run times. Furthermore, based on [23], the differences in the results fall in the typical range of uncertainty observed for validation against PWT data.

IV. Results and Discussion

This section presents the results, required for the submission to the CCP-WSI Blind Test Series 2. All simulations were performed on 23 cores of a dedicated server (Dell PowerEdge) with 48GB RAM and 24 Intel Xeon(R) E5-2440 processors, with 2.4GHz.

[4]The relative deviation is defined as: $(\text{Turbulent} - \text{Laminar}/\text{Laminar}) \cdot 100\%$

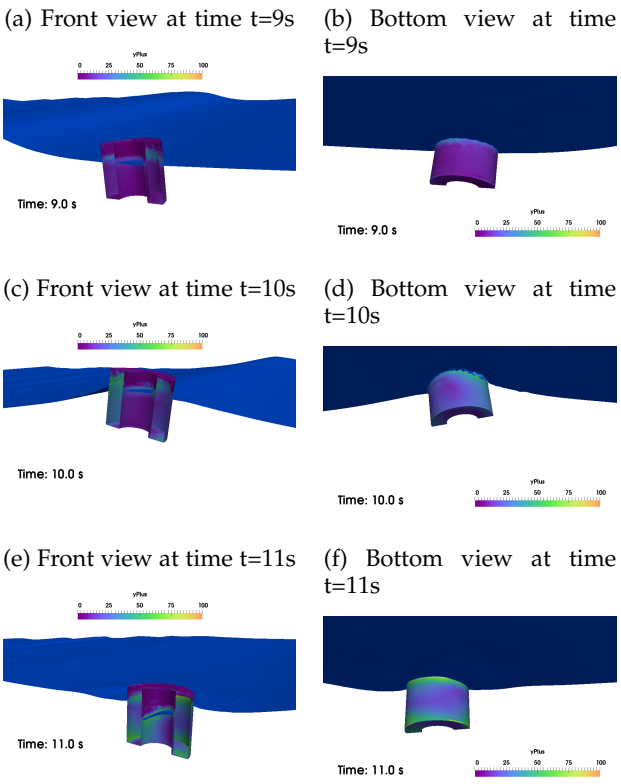

Fig. 12. Screen–shots, showing the y^+ values on geometry G2, at different time instances, immediately before (9s), at (10s), and immediately after the focused wave crest (11s)

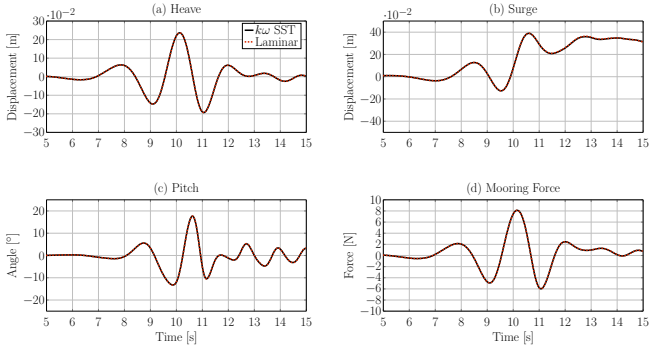

Fig. 13. Translational (heave and surge) and rotational (pitch) motion, as well as the mooring force time traces for G2, exposed to wave 3BT2, with and without turbulence modelling

TABLE V
RELATIVE DEVIATION, INDUCED BY TURBULENCE, AT THE PEAKS OF THE HEAVE, SURGE AND PITCH MOTION, AS WELL AS MOORING FORCE; GEOMETRY G2

		1BT2	2BT2	3BT2
Heave	[%]	< -0.1	< 0.1	0.1
Surge	[%]	-2.0	-1.7	-2.7
Pitch	[%]	1.2	2.7	3.9
Mooring Force	[%]	-0.2	-0.1	-0.24

H. Wave Calibration

For the present study, the maximum number of calibration iteration steps was set to 10. Fig. 14 shows

the target (solid black line) and resulting wave time trace (dashed red line) for the ten different calibration iterations. The target wave trace is defined as the experimental FSE, measrued during wave-only experiments, at the intended device location. It is assumed that the intended device location is the significant spatial location, in which the wave profile must be captured in order to accurately model the WSI. The root-mean-square error (RMSE) between the target and the resulting wave, for 1BT2, over the ten calibration iterations is plotted in Fig. 15.

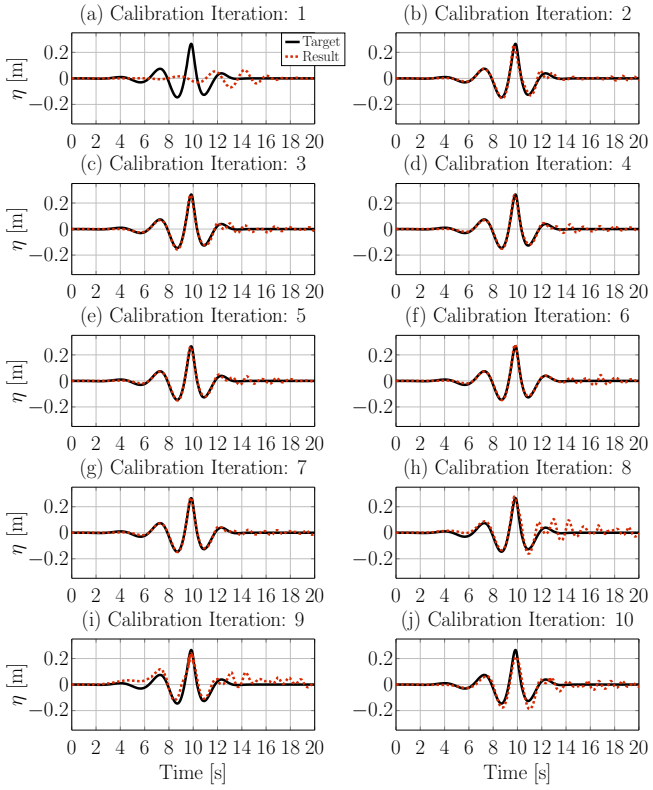

Fig. 14. Time traces of the target (solid black line) and resulting (dashed red line) FSE, η, for 10 calibration iterations

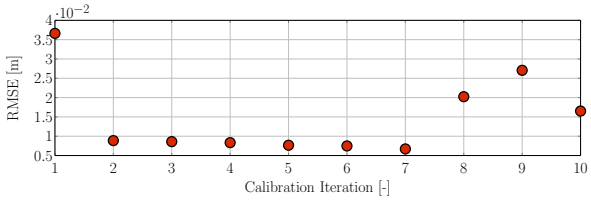

Fig. 15. RMSEs between target and resulting wave time traces over 10 calibration iterations

From Figs. 14 and 15, it can be seen that a relatively accurate representation of the target wave can be achieved after the second calibration iteration. The minimum RMSE value (6.7E-3 m) is achieved after 7 calibration iterations. For any further calibration iteration, the RMSE increases due to high frequency oscillations, which are introduced by the frequency-domain based calibration methodology.

Table VI lists the achieved minimum RMSE for waves 1BT2–3BT3. The corresponding time traces, used for all subsequent simulations are plotted in Fig. 16, together with the target waves.

TABLE VI
MINIMUM VALUES OF THE RMSE BETWEEN TARGET AND RESULTING WAVE TIME TRACES

		1BT2	2BT2	3BT2
Minimum RMSE	[m]	6.7E-3	8.3E-3	9.5E-3
No. of iterations with mininum RMSE	[-]	7	8	5

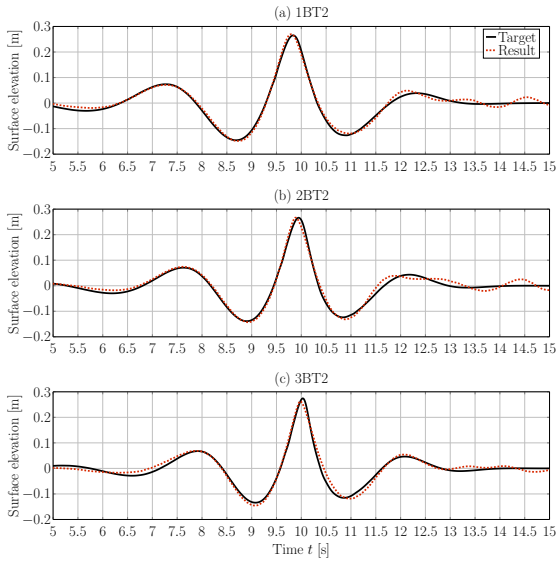

Fig. 16. FSE with minimum RMSEs and the target waves

For the submission to the blind test comparison, a number of criteria have to be considered for the assessment of the FSE time traces, as well as the motion and mooring force signals. These are: peak values, preceding trough depth, rising time, peak frequency, peak single-sided variance density, spectral bandwidth and the execution time (details on the definition of the assessment criteria are given in [6], which are, for brevity, omitted here). For the FSE of waves 1BT2–1BT3, the results for the above mentioned assessment criteria are listed in Table VII. Additionally, since the experimental data for the wave only test cases is provided, the assessment criteria are evaluated for the experimental data, and the relative difference between the experimental and numerical data is calculated[5] and listed in Table VII. Differences between the numerical and experimental FSE signals can be observed, with overall relative deviations of the order of $\mathcal{O}(10\%)$. While the peak and trough values generally show good agreement, with errors of the order of $\mathcal{O}(2\%)$, the rising time, as well as the spectral characteristics, show comparably larger errors. However, compared with other CNWT validation studies, the fit between the CNWT and PWT is satisfying [23].

[5]The relative deviation is defined as $(\text{Num.}-\text{Exp.}/\text{Exp.}) \cdot 100\%$

TABLE VII
RESULTS FOR BLIND TEST SUBMISSION: FSE AT WG 5

		Num.	Exp.	Relative Deviation
1BT2				
Peak value	[m]	0.270	0.265	1.9%
Preceding trough depth	[m]	-0.148	-0.146	1.7%
Rising time	[s]	1.08	1.16	-6.9%
Peak frequency	[s^{-1}]	0.380	0.367	3.5%
Peak single-sided variance density	[m^2 s]	0.313	0.327	-4.4%
Spectral bandwidth	[s^{-1}]	0.170	0.164	3.7%
Execution time of simulation	[s]	11368.4	–	–
2BT2				
Peak value	[m]	0.268	0.266	0.7%
Preceding trough depth	[m]	-0.141	-0.139	1.7%
Rising time	[s]	0.98	1.04	-5.8%
Peak frequency	[s^{-1}]	0.420	0.407	3.3%
Peak single-sided variance density	[m^2 s]	0.250	0.255	-2.1%
Spectral bandwidth	[s^{-1}]	0.170	0.177	-4.0%
Execution time of simulation	[s]	11466.1	–	–
3BT2				
Peak value	[m]	0.267	0.274	2.4%
Preceding trough depth	[m]	-0.144	-0.134	-7.3%
Rising time	[s]	0.92	0.94	2.1%
Peak frequency	[s^{-1}]	0.452	0.446	-1.4%
Peak single-sided variance density	[m^2 s]	0.201	0.202	0.6%
Spectral bandwidth	[s^{-1}]	0.216	0.190	13.6%
Execution time of simulation	[s]	11264.1	–	–

I. Wave structure interaction

For the WSI simulations, the same assessment criteria hold, as for the wave only test cases. The results for G1 are presented in Section IV-I1, and G2 in Section IV-I2. Since the experimental reference data are, at the time of writing, undisclosed, this section contains only the numerical results.

1) Geometry 1: For G1, the results for the assessment criteria for waves 1BT2–3BT2 are listed in Table VIII. The evaluated data sets are the time traces of the translational (heave and surge) and rotational (pitch) motion, as well as the mooring force time traces. The time traces of the motion and force data sets are plotted in Figs. 17–19, for waves 1BT2–3BT3, respectively. The according variance density plots are shown in Figs. 20–22, for waves 1BT2–3BT3, respectively.

Figs. 17–19 show that the heave motion and mooring force closely follow the trajectory of the focused wave FSE. Similarly, the surge motion follows the trajectory of the focused wave FSE; however, after the peak, the subsequent trough depth is much smaller, relative to the peak value, compared to the heave motion and mooring force signal. Remarkably, the time trace for the pitch motion does not follow the trajectory of the focused wave FSE. After the peak, the pitching motion of the WEC structure does not decay, but the body oscillates around its pitch equilibrium position.

From the variance density plots, shown in Figs. 20–22, a similar trend in the results, compared to the time traces, can be found. The heave motion and mooring force show a similar peak frequency. For the pitch motion, the peak frequency is slightly shifted, compared to the peak frequency of the heave motion and mooring force; however, a second peak can be observed for the pitch variance density, coinciding with the peak frequency of the heave motion and mooring force. For surge motion, the variance density plots for all three waves show non-zero values at $f = 0$Hz. The non-zero values stem from the non-zero mean of the signal (see Figs. 17–19).

TABLE VIII
RESULTS FOR BLIND TEST SUBMISSION: G1

		1BT2	2BT2	3BT2
Heave				
Peak value	[m]	0.242	0.232	0.223
Preceding trough depth	[m]	-0.143	-0.136	-0.139
Rising time	[s]	1.14	1.06	1.04
Peak frequency	[s^{-1}]	0.380	0.413	0.446
Peak single-sided variance density	[m^2 s]	0.311	0.247	0.196
Spectral bandwidth	[s^{-1}]	0.170	0.184	0.230
Execution time of simulation	[s]	38797.8	38968.2	39131.9
Surge				
Peak value	[m]	0.365	0.360	0.374
Preceding trough depth	[m]	-0.164	-0.146	-0.129
Rising time	[s]	1.16	1.08	1.08
Peak frequency	[s^{-1}]	0.367	0.387	0.387
Peak single-sided variance density	[m^2 s]	0.464	0.343	0.247
Spectral bandwidth	[s^{-1}]	0.144	0.151	0.223
Pitch				
Peak value	[°]	16.580	20.508	21.437
Preceding trough depth	[°]	-11.369	-13.414	-14.396
Rising time	[s]	0.82	0.78	0.8
Peak frequency	[s^{-1}]	0.754	0.708	0.734
Peak single-sided variance density	[$°^2$s]	2149.1	3845.3	3754.1
Spectral bandwidth	[s^{-1}]	0.164	0.177	0.177
Mooring Force				
Peak value	[N]	8.196	7.901	7.623
Preceding trough depth	[N]	-4.770	-4.555	-4.631
Rising time	[s]	1.16	1.08	1.02
Peak frequency	[s^{-1}]	0.374	0.413	0.440
Peak single-sided variance density	[N^2 s]	353.6	276.47	217.92
Spectral bandwidth	[s^{-1}]	0.177	0.177	0.230

2) Geometry 2: For G2, the time traces of the motion and force data sets are plotted in Figs. 23–25, for waves 1BT2–3BT3, respectively. The according variance density plots are shown in Figs. 26–28, for waves 1BT2–3BT3, respectively.

The motion and force time traces, plotted in Figs. 23–25 show similar characteristics, compared to the time traces for geometry G1. The variance density plots for G2, see Figs. 26–28, show more significant differences, compared to G1. While, for the surge motion, the variance density plots for all three waves show non-zero values at $f = 0$Hz, as in the case of G1, two significant peaks can be observed at $f > 0$Hz for all three waves. For the pitch motion, the significant peak is, again, shifted with respect to the peak of the heave motion and mooring force. However, the second peak for the pitch motion at lower frequencies, as found for G1, is dramatically suppressed for G2. The differences in the surge and pitch motion, compare to G1, highlight the influence of the sharp-cornered structure and the moon-pool.

V. CONCLUSION

This paper presents the CNWT used for the authors' contribution to the CCP-WSI Blind Test Series 2. The results of the spatial and temporal convergence are consistent with results found in the literature [23], and similar pitfalls as in [24] are found for the appropriate modelling of turbulence. A recently developed self-calibrating impulse source wave maker proves to be able to generated the desired focused wave with satisfying accuracy, with relative deviations to the target

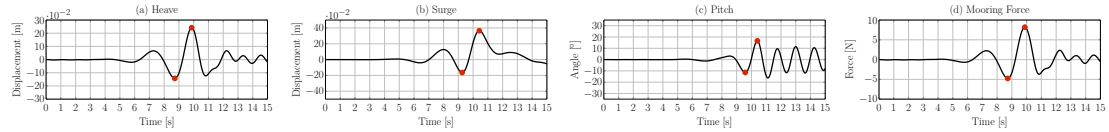

Fig. 17. Structure motion and mooring force time traces; G1, 1BT2

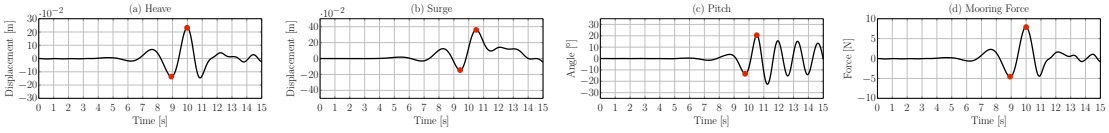

Fig. 18. Structure motion and mooring force time traces; G1, 2BT2

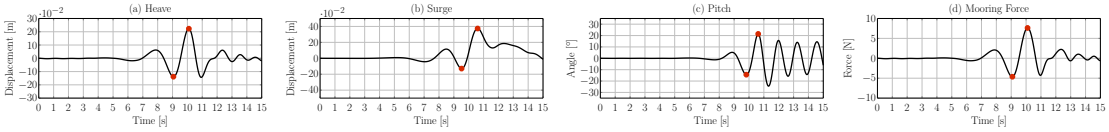

Fig. 19. Structure motion and mooring force time traces; G1, 3BT2

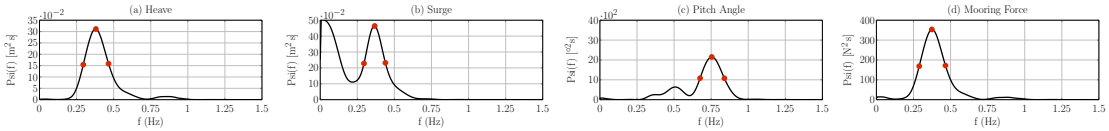

Fig. 20. Structure motion and mooring force variance density; G1, 1BT2

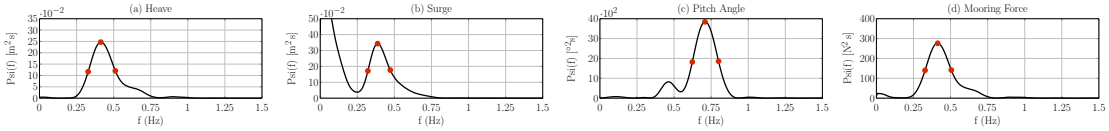

Fig. 21. Structure motion and mooring force variance density; G1, 2BT2

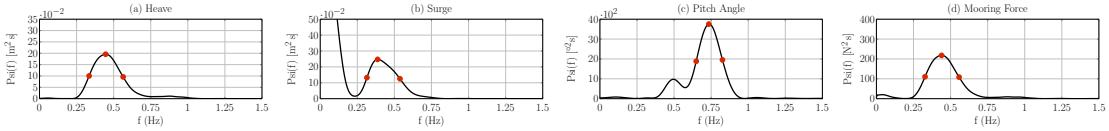

Fig. 22. Structure motion and mooring force variance density; G1, 3BT2

TABLE IX
RESULTS FOR BLIND TEST SUBMISSION: G2

		1BT2	2BT2	3BT2
Heave				
Peak value	[m]	0.239	0.224	0.216
Preceding trough depth	[m]	-0.140	-0.134	-0.138
Rising time	[s]	1.18	1.08	1.02
Peak frequency	[s^{-1}]	0.380	0.407	0.439
Peak single-sided variance density	[m^2 s]	0.330	0.278	0.214
Spectral bandwidth	[s^{-1}]	0.164	0.170	0.249
Execution time of simulation	[s]	40381.8	39889.0	39697.1
Surge				
Peak value	[m]	0.359	0.356	0.370
Preceding trough depth	[m]	-0.147	-0.124	-0.113
Rising time	[s]	1.2	1.1	1.1
Peak frequency	[s^{-1}]	0.308	0.459	0.479
Peak single-sided variance density	[m^2 s]	0.389	0.335	0.329
Spectral bandwidth	[s^{-1}]	0.216	0.111	0.105
Pitch				
Peak value	[°]	15.081	15.574	15.884
Preceding trough depth	[°]	-12.68	-14.733	-17.002
Rising time	[s]	0.9	0.9	0.88
Peak frequency	[s^{-1}]	0.564	0.577	0.564
Peak single-sided variance density	[$°^2$s]	2001.6	2878.3	3230.6
Spectral bandwidth	[s^{-1}]	0.170	0.164	0.164
Mooring Force				
Peak value	[N]	8.167	7.702	7.509
Preceding trough depth	[N]	-4.676	-4.475	-4.593
Rising time	[s]	1.2	1.1	1.04
Peak frequency	[s^{-1}]	0.374	0.407	0.439
Peak single-sided variance density	[N^2 s]	370.44	319.87	254.53
Spectral bandwidth	[s^{-1}]	0.170	0.164	0.223

focused wave height of the order of $\mathcal{O}(10\%)$. At the time of writing, a comparison of the WSI simulations is not possible, due to the non-disclosure of the experimental results.

ACKNOWLEDGEMENTS

This paper is based upon work supported by Science Foundation Ireland under Grant No. 13/IA/1886. The research in this paper was also supported by the Higher Education Excellence Program of the Ministry of Human Capacities in the frame of Water science & Disaster Prevention research area of Budapest University of Technology and Economics (BME FIKP-VÍZ).

REFERENCES

[1] P. Schmitt, C. Windt, J. Davidson, J. Ringwood, and T. Whittaker, "The efficient application of an impulse source wave maker to CFD simulations," *submitted to the Journal of Marine Science and Engineering*, 2019.

[2] M. Penalba, G. Giorgi, and J. V. Ringwood, "Mathematical modelling of wave energy converters: a review of nonlinear approaches," *Renewable and Sustainable Energy Reviews*, vol. 78, pp. 1188–1207, 2017.

[3] C. Windt, N. Faedo, M. Penalba, and J. Ringwood, "Evaluation of energy maximising control systems for the wavestar wave energy converter," in *Proceedings of the 2019 American Control Conference, Philadelphia, USA*, 2018.

[4] J. Davidson, C. Windt, G. Giorgi, R. Genest, and J. V. Ringwood, "Evaluation of energy maximising control systems for wave energy converters using OpenFOAM," in *OpenFOAM*. Springer, 2019, pp. 157–171.

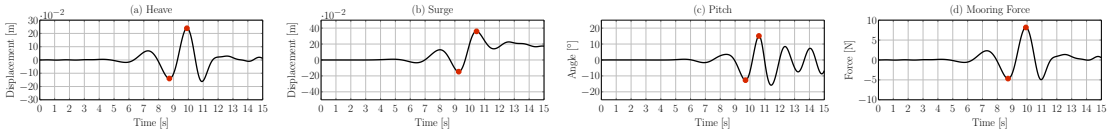

Fig. 23. Structure motion and mooring force time traces; G2, 1BT2

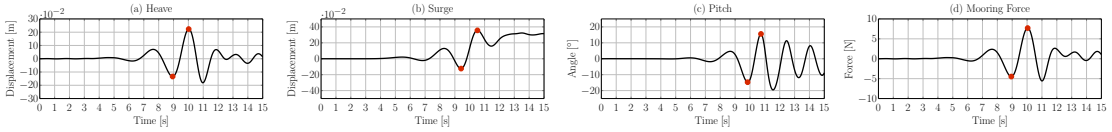

Fig. 24. Structure motion and mooring force time traces; G2, 2BT2

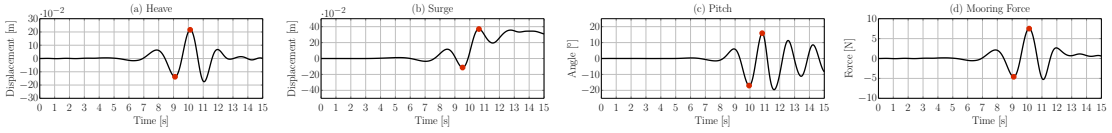

Fig. 25. Structure motion and mooring force time traces; G2, 3BT2

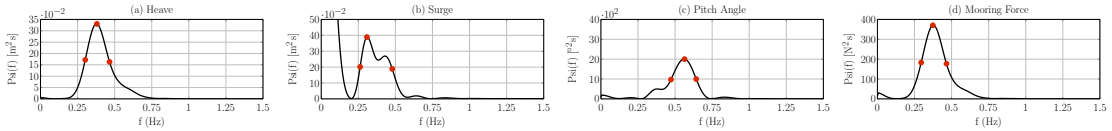

Fig. 26. Structure motion and mooring force variance density; G2, 1BT2

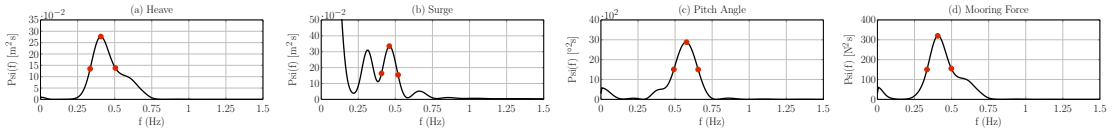

Fig. 27. Structure motion and mooring force variance density; G2, 2BT2

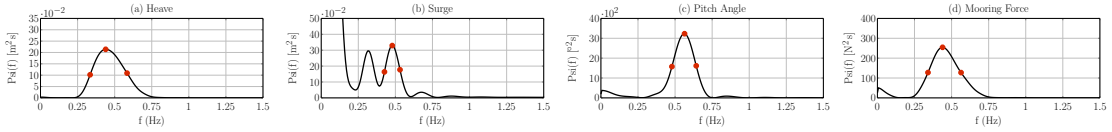

Fig. 28. Structure motion and mooring force variance density; G2, 3BT2

[5] E. Ransley, S. Yan, S. Brown, T. Mai, D. Graham, Q. Ma, P. Musiedlak, A. Engsig-Karup, C. Eskilsson, Q. Li, J. Wang, Z. Xie, V. Sriram, T. Stoesser, Y. Zhuang, Q. Li, D. Wan, G. Chen, H. Chen, L. Qian, Z. Ma, C. Mingham, D. Causon, I. Gatin, H. Jasak, V. Vukevi, S. Downie, P. Higuera, E. Buldakov, D. Stagonas, Q. Chen, J. Zang, and D. Greaves, "A blind comparative study of focused wave interactions with a fixed FPSO-like structure (CCP-WSI Blind Test Series 1)," *International Journal of Offshore and Polar Engineering (in Press)*, 2019.

[6] CCP-WSI website. (2018) Focused wave interactions with floating structures. [Online]. Available: https://www.ccp-wsi.ac.uk/blind_test_series_2

[7] ——. (2018) Focused wave interactions with floating structures. [Online]. Available: https://www.ccp-wsi.ac.uk/blind_test_series_3

[8] C. Windt, J. Davidson, P. Schmitt, and J. Ringwood, "Contribution to the ccp-wsi blind test series 3: Analysis of scaling effects of moored point-absorber wave energy converters in a cfd-based numerical wave tank," in *Proceedings of the International Society of Offshore and Polar Engineers (ISOPE) conference, 2019, Honolulu, USA*, 2019.

[9] H. G. Weller, G. Tabor, H. Jasak, and C. Fureby, "A tensorial approach to computational continuum mechanics using object-oriented techniques," *Computers in Physic*, vol. 12, pp. 620 – 631, 1998.

[10] The OpenFOAM Foundation Ltd. (2019) OpenFOAM foundation webpage. [Online]. Available: https://openfoam.org/

[11] C. W. Hirt and B. D. Nichols, "Volume of Fluid (VOF) Method for the Dynamics of Free Boundaries," *Journal of Computational Physics*, vol. 39, pp. 201–225, 1981.

[12] E. Berberović, N. P. van Hinsberg, S. Jakirlić, I. V. Roisman, and C. Tropea, "Drop impact onto a liquid layer of finite thickness: Dynamics of the cavity evolution," *Physical Review E*, vol. 79, pp. 036 306–1 – 036 306–15, 2009.

[13] CFD Direct. OpenFOAM v6 User Guide: 4.4 numerical schemes. Last accessed 11/12/2018. [Online]. Available: https://cfd.direct/openfoam/user-guide/v6-fvschemes/

[14] ——. OpenFOAM v6 User Guide: 4.5 solution and algorithm control. Last accessed 11/12/2018. [Online]. Available: https://cfd.direct/openfoam/user-guide/v6-fvsolution/

[15] H. K. Versteeg and W. Malalasekera, *An introduction to computational fluid dynamics: the finite volume method*. Pearson Education, 2007.

[16] T. Holzmann, "Mathematics, numerics, derivations and openfoam®," *Loeben, Germany: Holzmann CFD, URl: https://holzmann-cfd. de (visited on Jan. 23, 2019)*, 2016.

[17] C. Windt, J. Davidson, P. Schmitt, and J. V. Ringwood, "On the assessment of numerical wave makers for CFD simulations," *Journal of Marine Science and Engineering*, vol. 7, no. 47, 2019.

[18] J. Choi and S. B. Yoon, "Numerical simulations using momentum source wave-maker applied to RANS equation model," *Coastal Engineering*, vol. 56, pp. 1043–1060, 2009.

[19] S. Masterton and C. Swan, "On the accurate and efficient calibration of a 3D wave basin," *Ocean Engineering*, vol. 35, pp. 763–773, 2008.

[20] P. Schmitt and B. Elsaesser, "A review of wave makers for 3d numerical simulations," in *MARINE 2015 - Computational Methods in Marine Engineering VI, Rome*, 2015, pp. 437–446.

[21] E. Mansard and E. Funke, "The measurement of incident and reflected spectra using a least squares method," in *Proceedings of the International Conference on Coastal Engineering, Sydney, Australia*. American Society of Civil Engineers (ASCE), 1980, pp. 154–172.

[22] F. R. Menter, "Improved Two-equation kω Turbulence Models for Aerodynamic Flows," NASA Technical Memorandum TM-103975, Tech. Rep., 1992.

[23] C. Windt, J. Davidson, and J. Ringwood, "High-fidelity numerical modelling of ocean wave energy systems: A review of CFD-based numerical wave tanks," *Renewable and Sustainable Energy Reviews*, vol. 93, pp. 610 – 630, 2018.

[24] P. Schmitt and B. Elsässer, "The application of froude scaling to model tests of oscillating wave surge converters," *Ocean Engineering*, vol. 141, pp. 108–115, 2017.